Microstructure and anisotropic tensile performance of 316L stainless steel manufactured by selective laser melting

Lin Wang

Department of Civil Engineering, Hefei University, Anhui, China
linw@smu.edu, http://orcid.org/0000-0002-6481-2409

ABSTRACT. The selective laser melting (SLM) technology is widely used to manufacture 316L stainless steel (SS) components for industrial applications. To understand the microstructure and the mechanical properties of additively manufactured 316L alloy, bulk materials were fabricated in longitudinal and transverse directions from which subset tensile specimens were then machine. Bulk materials were subjected to porosity detection with X-ray computed tomography and texture analysis with electron backscatter diffraction (EBSD). Microstructural investigations reveal that the SLM-built specimens had a porosity of 1.87%, and a preferential {110} orientation parallel to the build direction. The transverse specimens show significantly better properties in elastic modulus E (215.1±4.7GPa), yielding stress σ_y (548.2±8.3MPa) and ultimate tensile strength UTS (705.6±2.9MPa) than the longitudinal ones (E of 175.9±9.8GPa, σ_y of 495.3±15.5 and UTS of 608.8±3.6MPa). The anisotropic mechanical performance was attributed to the preferential {110} texture caused by thermal conditions during manufacturing and the embedded voids due to insufficient melting. A three-parameter Weibull distribution was adopted to further describe the mechanical anisotropy of SS316L based on stochastic experimental measurements. Fractography indicated the existence of manufacturing defects that drive to premature failure of SS316L specimens—around half SS316L specimens failed of elongation less than 0.4.

KEYWORDS. Selective laser melting; 316L stainless steel; Porosity; Mechanical anisotropy; Weibull distribution.

INTRODUCTION

S elective laser melting (SLM) is an additive manufacturing (AM) technique whereby structures are built in a repeated layer-wise fashion via selectively or localized melting using high-intensity laser energy and solidification from metallic powder bed feedstock. Compared to conventional subtractive manufacturing methods, the key benefit of SLM is the ability to rapidly fabricate customized mechanical components of complex geometry, with the potential for improved

efficiency and functionality [1]. Consistently qualified mechanical properties of additively manufactured material are necessary to fully realize the function of customized components [2]. However, uncertainty in the mechanical performance of built material prevents the mass adoption of AM technique in safety-critical environments [3].

Additively manufactured alloys, in particular, stainless steel 316L have been reported to exhibit anisotropic mechanical performance in nature [4-7]. Many factors are reported responsible for the mechanical anisotropy of additively fabricated SS316L alloys. Crystallographic texture of AM alloys in characteristics as grain size, shape, orientation, and aspect ratio directly affects the mechanical properties of SLM SS316L, such as yield and tensile strength [7-10]. Considering the rapid heating and cooling cycle of successive layers during the SLM process, the microstructures of manufactured alloys are found highly dependent on the process parameters, such as laser power, scanning speed, and scanning strategies [4-7, 9]. The mechanical properties of SLM fabricated 316L stainless steel were found significantly anisotropic, which is attributed to the anisotropic mesostructured [7]. Recently, deformation mechanisms, mainly dislocation slip and twinning combined with crystal texture are thought responsible for the directional dependency of material behavior [10-12]. The layer interface is attributed as another frequently mentioned cause since oxidation, inclusions and other defects are easier to form in this region as a consequence of layer-by-layer manufacturing [5, 6]. Residual stress caused by thermal gradient during processing is also contributing to the anisotropy of AM SS316L [13]. Furthermore, the final mechanical properties of a fabricated alloy are also influenced by its porosity, especially when high scanning speed, high process efficiency, and low energy density are utilized during fabrication [1, 4, 6]. Image processing based on X-ray computed tomography (CT) was adopted to evaluate the porosity in SLM parts [14, 15]. However, quantitative characterization of the porosity of SLM 316L is seldomly reported. Based on the state of research, a further investigation about the underlying cause of anisotropy of SLM SS316L is required. The objective of the current work is to investigate the effect of building direction on the mechanical performance of SLM-built 316L stainless steel under uniaxial tension. X-ray CT and texture analysis with electron backscatter diffraction (EBSD) were used to characterize the material, and to relate the microstructural and crystal morphology to the mechanical properties of SLM built 316L stainless steel. A three-parameter Weibull distribution was used to statistically evaluate the mechanical anisotropy of SLM 316L from stochastic experimental data.

MATERIAL AND METHODS

Material and specimen

A commercial laser powder bed fusion system SLM280 (Wiiboox, China) was utilized to produce the SS316L parts. The gas-atomized SS316L powder of apparent density 4.67g/cm³ and particle size 16.7±8.6µm was adopted as feedstock for metallic parts fabrication with chemical composition listed in Tab. 1. The process parameters for all specimens were set as follows: nominal layer thickness 30µm, laser power 100W, laser beam diameter 100µm, hatching spacing 100µm, scanning speed 1.2m/s. The volume-based energy density E_V (J/mm³) is defined in Eq. (1), where P is the laser power (W), v is the scanning speed (mm/s), h is the hatching spacing and t is the layer thickness (mm).

$$E_V = \frac{P}{v \times h \times t} \tag{1}$$

The energy density used to fabricate the SS316L specimen was calculated as 27.78J/mm³. An alternating scanning strategy by rotating 90° in successive layers was applied. The laser melting process was conducted in an argon gas atmosphere building chamber with an oxygen content of no more than 0.5%.

The SS316L metallic parts were oriented in either longitudinal or transverse directions during processing, see Fig. 1a. The building orientation of the longitudinal metallic part coincides with the axial loading direction, while the transverse part has a building direction perpendicular to the tensile loading force. After manufacturing, the subsize tensile specimens were directly sliced from the additively manufactured bulk parts with thickness 1mm by electrical discharge machine technique. The surface roughness of SS316L tensile specimens after electrical discharge machining in average roughness R_a was measured as 5.6±0.3µm. The detailed geometry of tensile specimens is given in Fig. 1b.

C	Mn	Si	Cr	Ni	Mo	Fe
0.007	1.5	0.6	17.1	13	2.6	Balance

Table 1: Chemical composition of stainless steel 316L powder.

Microstructural characterization

Four SS316L metallic blocks (9mm×4mm×8mm) were also additively manufactured with the same process parameters as the bulk parts. These four blocks were inspected by a microfocus X-ray CT system XT H225ST (Nikon Group, Japan) of parameters as 140kV voltage and 220μA current to produce a series of grayscale images with 16-bit intensity ranges. The voxel resolution of scanned images was determined as 8.9μm. Based on the CT images, the interior porosity or void characteristics of the fabricated SS316L was quantified. The microstructure of the SLM manufactured SS316L part was inspected by an SEM SU8010 (Hitachi Ltd, Japan) integrated EBSD technique with acceleration and extraction voltages as 30 and 5.0 keV, respectively. The step size for EBSD measurements was 3.0μm.

Tensile test

Uniaxial tension tests of SLM manufactured SS316L specimens in longitudinal and transverse directions were conducted on an Instron E1000 material test system (1000±0.1N) at room temperature (Fig. 2). The axial tensile loading of the tensile specimen was precisely controlled by a constant crosshead speed of 3mm/min, corresponding to a nominal strain rate of $1.25×10^{-2}$/s. In addition, four longitudinal and five transverse specimens were axially loaded at a lower speed (LS) as 0.03mm/mm or $1.25×10^{-4}$/s. The SS316L specimens were first stretched just beyond the yield point and unloaded to force level 20N, and then reloaded till complete separation.
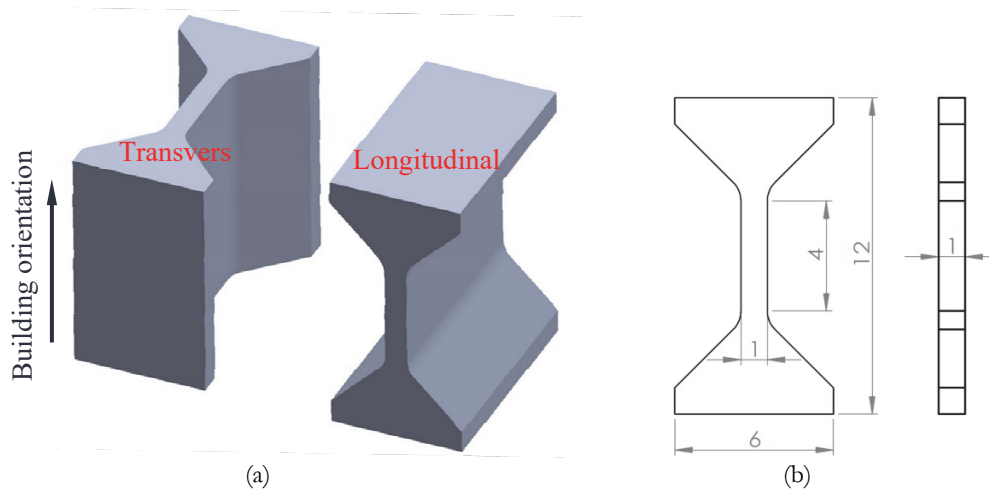

Figure 1: (a) Building orientations of SLM fabricated SS316L parts, (b) geometry of tensile specimen (mm).

The digital image correlation (DIC) technique was adopted in the tensile test for axial elongation and full-field deformation measurement. To facilitate DIC measurement, the surface of the SS316L specimen was decorated with fine black-to-white paint speckles with a spatial resolution of captured images as ~0.005 mm/pixel. High-quality digital images (2048×2048 pixels, 8 bit) of specimen surface during tensile testing were continuously captured by a CCD camera (acquisition rate 3fps). After testing, the captured images were processed by a non-contact DIC algorithm Ncorr [16] with subset radius and grid spacing as 20 and 2 pixels respectively for deformation measurement. The measurement error in axial strain is estimated to be about 0.05% at most based on the captured digital images prior to the test starting. The DIC measured axial tensile strain was synchronized in time with the applied axial loading recorded by the Instron E1000 machine to obtain the engineering stress-strain curves of SLM fabricated SS316L specimens. The engineering stress is calculated by dividing the applied axial load by the measured cross-sectional area of the tensile specimen.

RESULTS AND DISCUSSION

Microstructure

Image processing and reconstruction for pore or void quantification were conducted after the X-ray CT scanning of AM SS316L parts using software MATLAB (The MathWorks, Inc, Massachusetts, U.S.) and ImageJ (NIH, Maryland, U.S.). Digital images were first processed by histogram stretching and nonlocal mean 3D filtering to enhance the contrast and remove the possible noise. SS316L part was then segmented with a threshold filtering from the processed

digital image series. The threshold value was manually calibrated by comparing images before and after threshold filtering to show the best objective identification. Quantitative information analysis of porosity defects such as pore volume was obtained from the binary images after threshold filtering-based segmentation. Pores are defined as void surrounded by modeling material without connection with others.
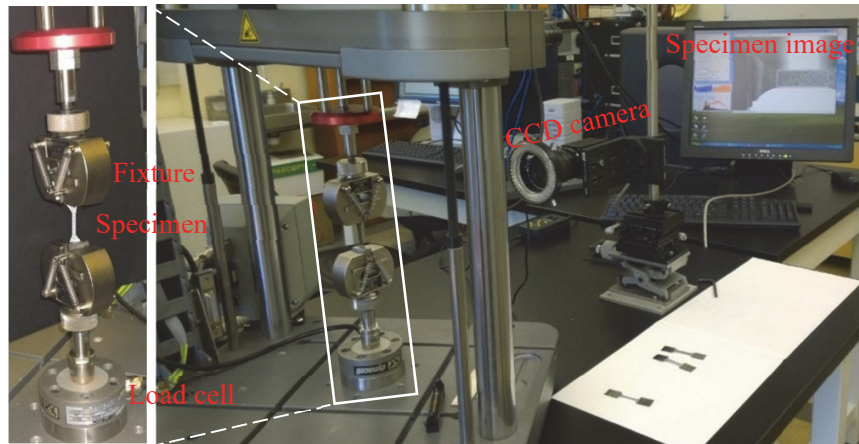

Figure 2: Setup of tensile test.

Following the aforementioned image process routine, the void microstructures within four AM SS316L parts are shown in Fig. 3a. For a better visibility, intensities are adjusted with pores displayed as red, bulk SS316L part as transparent. Based on X-ray CT images, a total of 3047 voids were found within four SS316L parts. The defect voids in the microstructure are distributed mainly within the layer interface. These pores show similar characteristics of pores caused by the lack-of fusion due to insufficient energy density to completely melt the stainless-steel powder during the SLM processing [17, 18]. Previous research indicates a volumetric energy density to guarantee a fully dense specimen ranges between 60 and 120J/mm^3[19]. The one used in the present study for specimen fabrication was much lower at 27.78J/mm^3. The metallic powder may not be fully melted under such energy density and therefore, the voids are easy to form between neighboring scanning paths, as shown in Fig. 3a. The presence of interlay porosity would reduce the loading bearing area and in turn yield smaller elastic modulus and strength [3, 4, 7, 10]. The majority of voids are approximated to be ellipsoid in shape. The remaining voids generally have irregular shapes similar to linked ellipsoid. The distribution of void radius is statistically obtained using the circle equivalent method and described in Fig. 3b. The average radius of all voids is 8.74±9.47μm, with 2.30μm and 90.97μm for the smallest and largest voids respectively. Most of the voids are quite small, i.e., 88.25% of the voids are smaller than the average radius of SS316L powder as 16.7μm. The porosity of four SLM fabricated parts is calculated as 1.87% on average. The crystallographic morphologies as grain size and orientation of SLM fabricated SS316L were evaluated and shown in Fig. 4. The EBSD mappings were scanned along the building-transverse plane. The colors in EBSD micrographs represent the grain orientation with respect to the building direction. As illustrated in Fig. 4a, the microstructure of scanned specimen exhibits elongated or columnar grains roughly parallel to the building direction with a large fraction of grain in green color. The grains in the transverse direction have an equiaxed shape. This microstructural morphology attributes to cellular solidification, depending on the thermal gradient in the liquid *G* and the solidification front growth rate *R* during the layer-wise additive manufacturing process [10]. The ratio *G* to *R* controls the morphology of stainless-steel alloy, while the product *G×R* dominates the cooling rate and the refinement in the microstructure. The heat conduction as thermal gradient and cooling rate in the building direction is typically higher than the one in the layer plane, which predominates the growth of both columnar and equiaxed grains [20]. Relatively weak material properties are usually achieved in the same direction with the orientation of undesired columnar grains [3-6, 9, 11, 17, 19, 20]. The average grain size of SLM SS316L in the scanned plane is measured as 23.19μm and 55.03μm in transverse and longitudinal directions, respectively. The inverse pole figure of the same plane as shown in Fig. 4b indicates the SLM 316L has a strong {110} micro-texture evident with respect to the part growth direction. The inhomogeneity in microstructural grains may drive to anisotropic mechanical response of SLM fabricated specimens.

Tensile testing

The engineering stress-strain curves of additively manufactured 316L specimens under uniaxial tension are shown in Fig. 5. For comparison, the minimum UTS 485MPa and elongation or strain to failure ε_f 0.4 of wrought SS316L material per ASTM

A240 standard are also included in Fig.5 as dashed lines. The stress-strain curves of SS316L specimens of the same building orientation and the same loading speed generally follow the similar trend till the onset of diffuse necking point, determined by Considère criterion as

$$\sigma = \frac{d\sigma}{d\varepsilon} \qquad (2)$$

The ultimate tensile strength is measured from the same point. The specimens behave uniformly within the region between the points of yielding and the onset of the diffuse neck. The strain hardening rate of the transverse specimens is larger than the longitudinal specimen until the uniform elongation point is determined by Eq. (2). Beyond the onset of diffuse necking till the complete separation of the tensile specimen, the stress-strain curves diverge significantly from each other. Fig. 5 indicates that the measured UTS of SLM SS316L in both building directions tested under two loading speeds is larger than the reference value of wrought SS316L given in the ASTM A240 standard. However, around half of SS316L specimens (7 of 15 and 8 of 17 specimens fabricated in longitudinal and transverse directions, respectively,) fractured with elongation smaller than its reference value 0.4 under loading speed 3mm/min. The measured fracture strain of SS316L specimens tested under lower loading speed is beyond the reference value of wrought 316L. The experimental repeatability needs further evaluated since limited specimens were tested compared to higher loading speed. Tensile properties of SLM fabricated 316L specimens as elastic modulus E, yielding stress σ_y, UTS, and fracture strain ε_f extracted from the tensile tests are listed in Tab. 2. A substantial increment in elastic modulus E, yielding stress σ_y and UTS of transverse specimens is observed compared to longitudinal specimens at the same loading speed. In general, the comparison of tensile properties of SLM SS316L specimens reveals a strong inherent anisotropic characteristic in mechanical behavior dependent on building orientation.
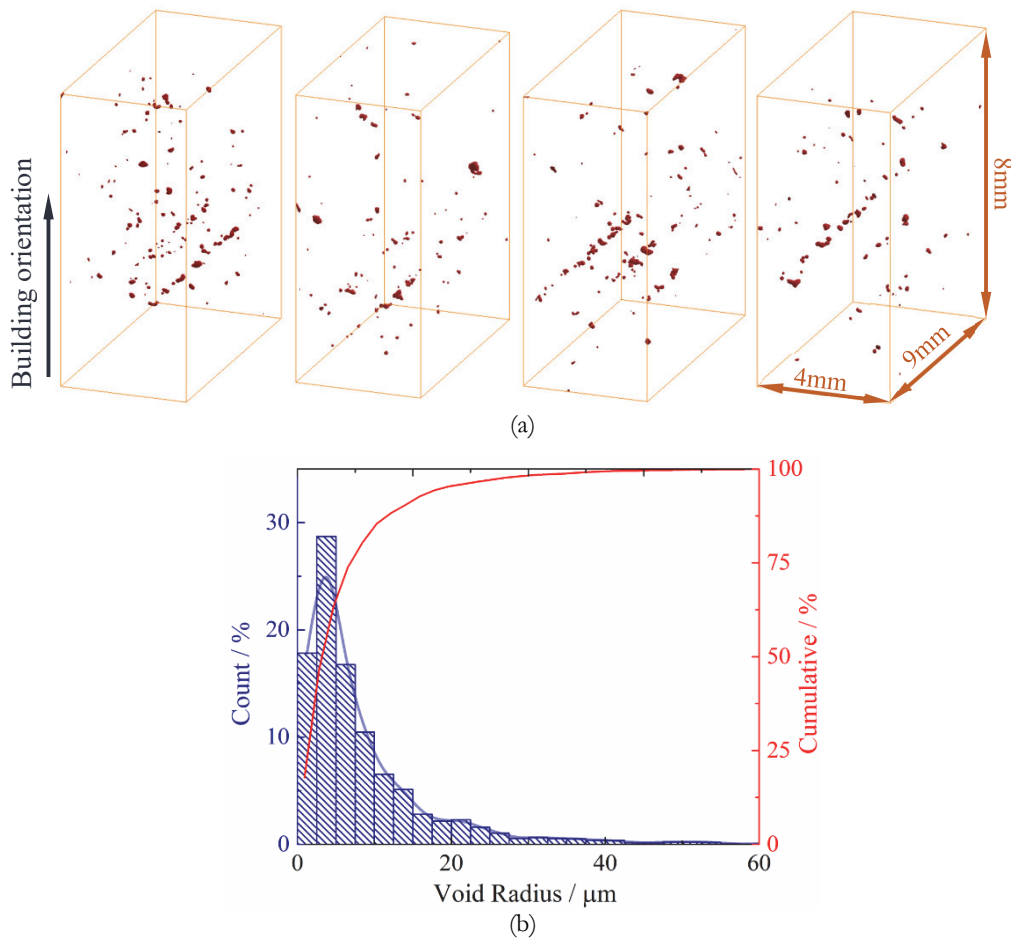

Figure 3: Microstructural voids (a) within four different printed SS316L parts and (b) statistical information.

The mechanical anisotropy attributes mainly to two major reasons. The preferential {110} texture correlated to building orientation as indicated in Fig. 4 is the leading cause. The longitudinal specimens have the elongated or columnar grains coincident with the loading direction of tensile testing. Meanwhile, the transverse specimens have generally equiaxial grains perpendicular to the tensile loading. As reported in [9, 11, 17, 19], an increased aspect ratio of columnar grain would decrease the yielding and tensile strength. Consequently, a material with equiaxed grains is accompanied by high dislocation and stacking fault density, which contributes to the improved yield stress and ultimate tensile strength, as demonstrated in Fig. 5 and Tab. 2. On the other hand, the embedded voids or defects resulting in reduced loading bearing area also have a noteworthy influence on the tensile performance of SLM 316L stainless steel specimens. As consisting of more layers than the transverse specimens, longitudinal specimens suffer more from the manufacturing defects.
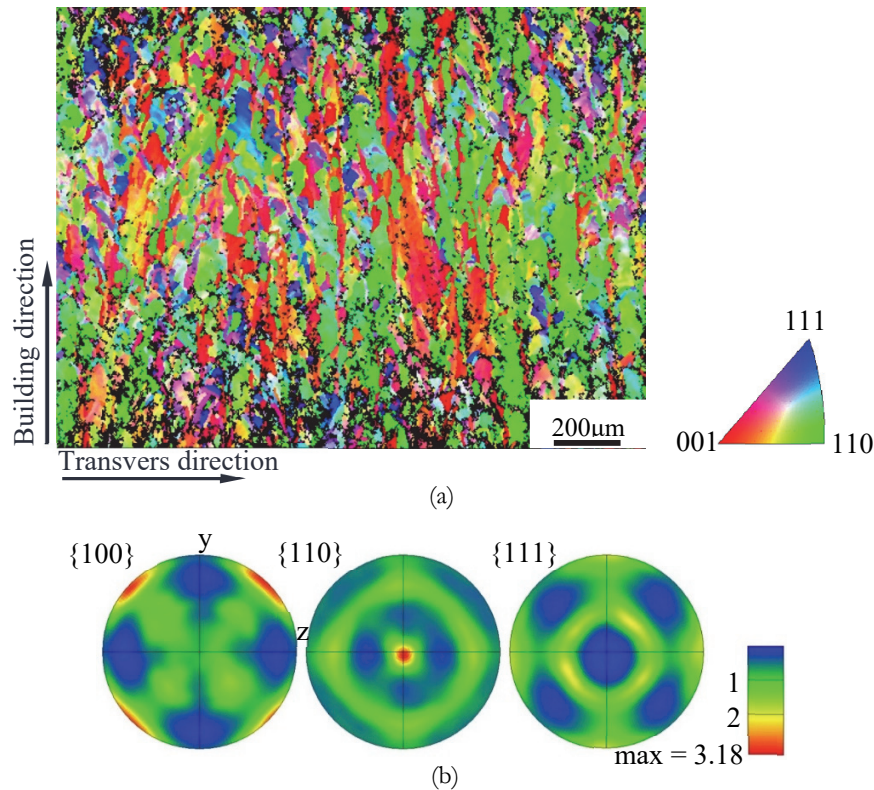

Figure 4: Measured microstructure as (a) EBSD and (b) inverse pole figure maps for SLM manufactured SS316L.

Due to the lack of consistency in the mechanical performance of the SLM SS316L specimen, empirical cumulative probability distribution for the elastic modulus E, yielding stress σ_y, UTS and fracture strain ε_f were determined using a three-parameter Weibull distribution. The Weibull distribution has been used to describe the stochastic mechanical properties of materials, like the tensile strength [2, 21], fracture toughness [22], elongation [23]. According to the Anderson-Darling metric, the Weibull distribution yields a superior goodness-to-fit compared to a Gaussian distribution for the statistical description of experimental variation. Sufficient data is essentially necessary to well calibrate the 3-parameter Weibull distribution [2, 24]. The 3-parameter Weibull cumulative distribution function follows:

$$P = 1 - e^{-(\frac{t-\gamma}{\eta})^{\beta}}$$

(3)

where the cumulative probability of failure P is a function of the variable t and three parameters: the Weibull modulus or shape parameter β to describe the general breadth, the scale parameter or characteristic value η, and the location parameter or threshold γ below which the probability is zero. The results reveal that datasets obtained from tensile tests under loading speed 3mm/min are able to uniquely determine the 3-parameter Weibull distribution. The tensile performance of specimens tested under 0.03mm/min was described by a 2-parameter Weibull distribution due to limited datasets. The cumulative probability distributions for the tensile properties of AM SS316L are shown in Fig. 6, and the parameter estimates for each of the databases are given in Tab. 3. The general trends of distributions are clear from the graphs and the accompanying

table. The 3-parameter Weibull distributions of elastic modulus E, yielding stress σ_y and UTS of longitudinal and transverse specimens tested at strain rate 1.25×10^{-2}/s separate from each other. The calibrated location parameter or threshold value γ listed in Tab. 3 shows that transverse specimens behave obviously better in elastic moduli E, yielding stress σ_y and UTS with statistical significance if compared with the longitudinal specimens. The distinct effect of building orientations on the tensile properties of fabricated SS316L specimens is observed again. As discussed above, the preferred grain orientation caused by the laser processing and the material porosity due to the scanning process are the two leading causes for the influence of building orientation.
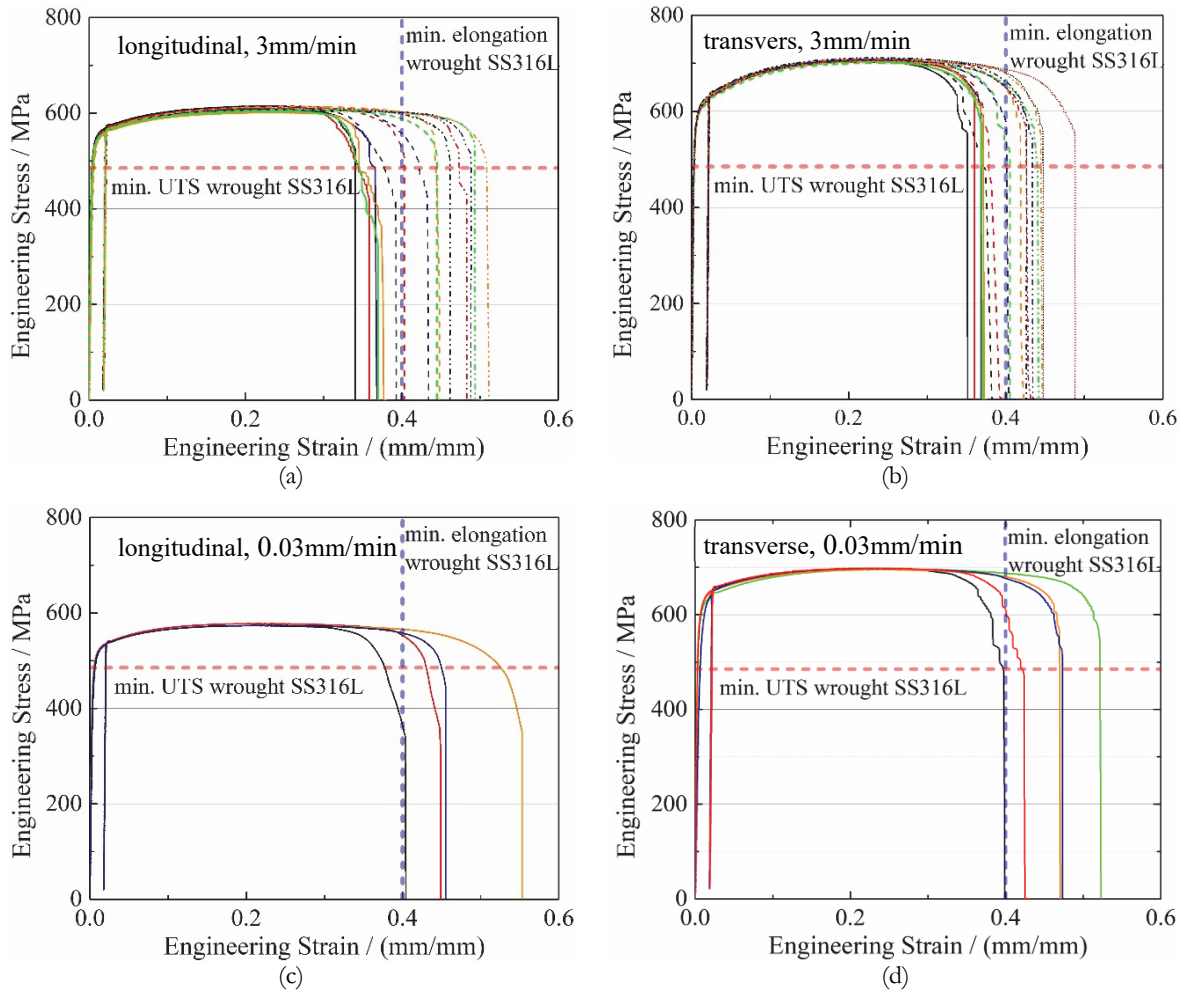

Figure 5: Tensile stress-strain curves of SS316L manufactured in (a) longitudinal and (b) transverse orientations at loading speed 3mm/min, and (c) longitudinal and (d) transvers orientations at loading speed 0.03mm/min.

Building Orientation	Loading Speed mm/min	Number of Test	Elastic Modulus GPa	Yielding Stress MPa	UTS MPa	Fracture Strain mm/mm
longitudinal	3	15	175.90±9.80	495.27±15.45	608.84±3.59	0.419±0.057
longitudinal	0.03	4	182.75±5.81	465.92±14.70	574.74±1.91	0.465±0.063
transvers	3	17	215.11±4.68	548.21±8.30	705.57±2.88	0.406±0.038
transvers	0.03	5	206.24±3.34	544.94±3.45	696.72±1.32	0.457±0.048

Table 2: Summary of mechanical properties of 316L stainless steel

The Weibull distributions of elastic modulus for 316L specimens tested at loading rates 1.25×10^{-4}/s and 1.25×10^{-2}/s are generally overlapped. Specimens with the same building orientation yield statistically identical elastic moduli tested under

different loading rates, since the elastic modulus of metal material is generally thought independent of strain rate [25]. An apparent influence of strain rate on the yielding stress and ultimate tensile strength is observed for SS316L specimens. More tests under low loading speed are needed to further evaluate the repeatability and to conform the strain rate effect on the tensile performance of SLM fabricated 316L material. On the other hand, the fracture strain ε_f of SS316L specimens measured in this research shows great stochastic, which is found insensitive to the building orientations and strain rate. In uniaxial tensile testing, the strain rate sensitivity is measured as the change in observed strength. Based on experimental measurements, the ultimate tensile strength of longitudinal and transverse SS316L specimens tested under strain rate 1.25×10^{-2}/s increase around 5.9% and 1.3%, respectively compared with the strength measured under strain rate 1.25×10^{-4}/s. The longitudinal specimens show a stronger effect of strain rate on the tested strength, as reported in [26].
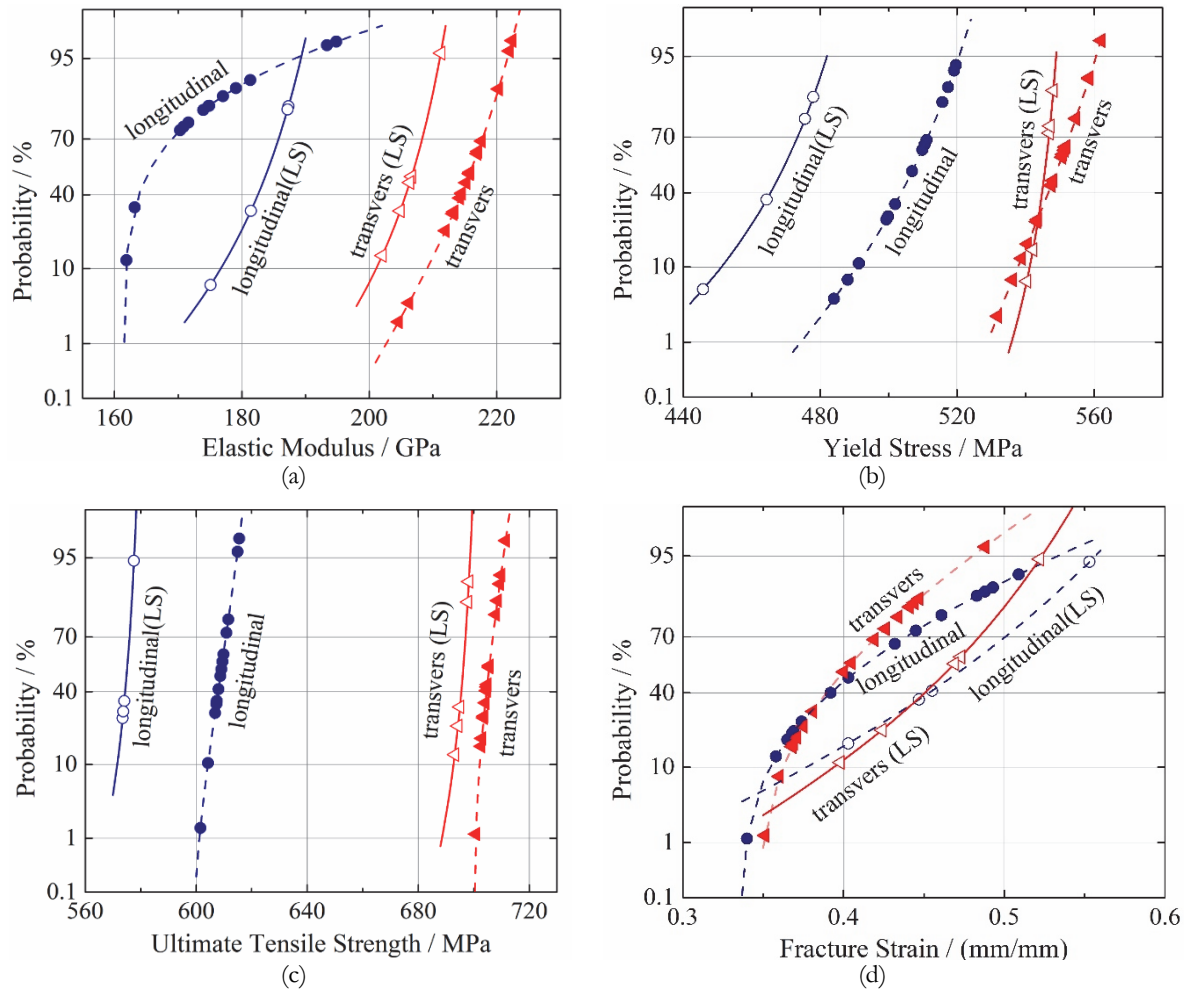

Figure 6: Cumulative probability distribution for the (a) elastic modulus, (b) yield stress, (c) ultimate tensile strength and (d) fracture strain of SLM manufactured SS316L.

Fractography of fracture surface
Statistical results offer the ability to identify atypical elongation performance, while fractography is able to diagnose possible reasons of premature failure. The fractographical characteristics of the fracture surface for one longitudinal specimen are examined in Fig. 7. The selected specimen failed with an elongation of only 0.36, much smaller than the average fracture strain of the longitudinal group. Extensive lack-of-fusion voids with a pronounced shear lip are observed from the fracture surface. The voids approximate about 9.6% of the reduced cross-section. The width of large voids ranges from 65μm to 193μm. Fig. 7b shows the embedded voids in specimens caused by the laser scanning process within the region of fracture initiation. Un-melted or partially melted powders are present within some large penetrating voids, as indicated in Fig. 7c and d caused by relatively low volume energy density. Fig. 7e and f show the typical ductile failure characterized as dense dimples in the central region of the fracture surface. The defects inside the tensile specimen, like the lack-of-fusion voids, un-melted

powder, and oxide particles complex, as observed in high magnification SEM images induce dramatic stress concentration around these defects, especially within the necking cross-section [7-12, 19, 26]. The presence of the aforementioned defects facilitates an easy cracking path and triggers the premature failure of the SLM SS316L specimen, which in turn drives the stochastic tensile performance of additively manufactured SS316L specimens.

Property	Specimen	Number of Tests	Shape Parameter (Weibull Modulus)	Scale Parameter (Characteristic Strength)	Location Parameter (Threshold Value)
		N	β	$\eta+\gamma$	γ
E / GPa	Longitudinal	15	0.71	167.31	161.56
	Transvers	17	8.86	217.01	181.61
	Longitudinal (low)	4	48.63	185.05	0*
	Transvers (low)	5	68.99	207.76	0*
σ_y / MPa	Longitudinal	15	11.28	509.75	443.92
	Transvers	17	4.87	550.03	514.63
	Longitudinal (low)	4	50.62	471.65	0*
	Transvers (low)	5	237.31	546.38	0*
UTS / MPa	Longitudinal	15	3.40	610.04	598.06
	Transvers	17	2.11	706.30	699.93
	Longitudinal (low)	4	316.36	575.65	0*
	Transvers (low)	5	389.60	696.72	0*
ε_f / %	Longitudinal	15	1.40	0.43	0.34
	Transvers	17	1.54	0.41	0.35
	Longitudinal (low)	4	8.60	0.49	0*
	Transvers (low)	5	11.80	0.48	0*

* Obtained from 2-parameter Weibull distribution as the threshold value cannot be uniquely determined.

Table 3: Parameters of Weibull distribution for tested SS316L.

CONCLUSION

In the present work, the microstructure and the tensile performance of the SLM fabricated 316L stainless steel were experimentally investigated with key observations as follows.

1. Through X-ray CT scanning, the voids inside fabricated SS316L material caused by low energy density were observed; EBSD analysis reveals a preferential {110} grain orientation parallel to the building orientation, correlating to the thermal gradient and the solidification rate during the layer-wise process of SLM.

2. The tensile properties of additively manufactured SS316L specimens were significantly anisotropic, which attributed to the preferential grain orientation and interlayer defects. The transverse specimen behaves better performance in elastic modulus, yield stress, and UTS compared to longitudinal specimens. The effect of strain rate on the UTS is stronger for longitudinal than transverse specimens.

3. A three-parameter Weibull distribution was found suitable to describe the stochastic tensile performance of SLM 316L stainless steel. The mechanical anisotropy and strain rate effect of SS316L specimens are obviously distinct based on the cumulative probability distribution.

4. High magnification SEM observation revealed that the presence of void, un-melted powder, and other defects lead to dramatic stress concentration, trigger the premature fracture initiation and facilitate an easy path for crack growing, which in turn drives in stochastic tensile performance of SLM SS316L specimens.
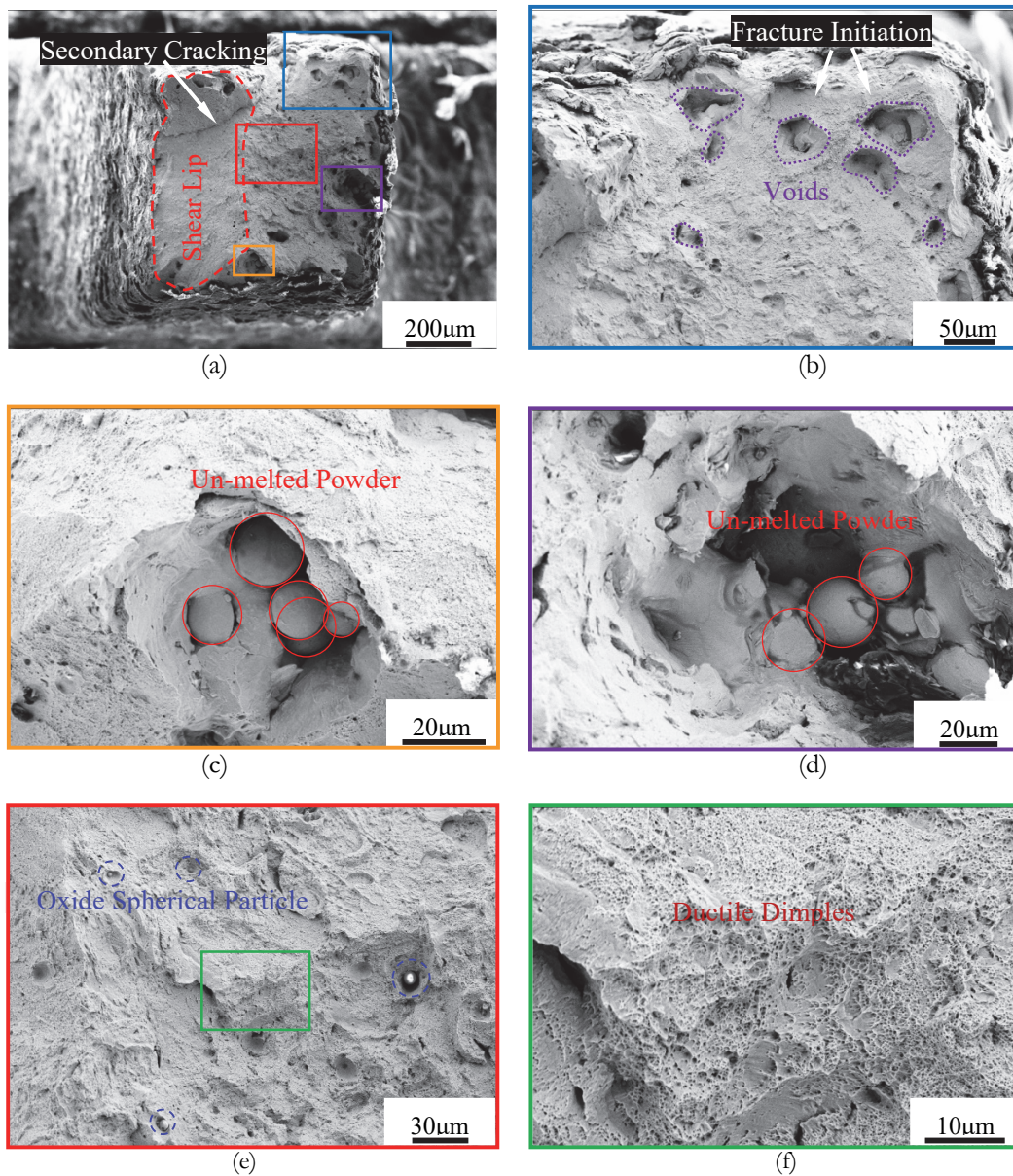
Figure 7: Fractography of (a) whole fracture surface, (b) fracture initiation site, (c) and (d) un-melted powder defects, (e) ductile failure and (f) close-up ductile dimples for SLM manufactured SS316.

REFERENCES

[1] Frazier, W. E. (2014). Metal additive manufacturing: a review. J. Mater. Eng. Perform, 23(6), pp. 1917-1928. DOI: 10.1007/s11665-014-0958-z.

[2] Salzbrenner, B. C., Rodelas, J. M., Madison, J. D., Jared, B. H., Swiler, L. P., Shen, Y. L. and Boyce, B. L. (2017). High-throughput stochastic tensile performance of additively manufactured stainless steel. J. Mater. Process. Technol., 241, pp.1-12. DOI: 10.1016/j.jmatprotec.2016.10.023.

[3] Seifi, M., Salem, A., Beuth, J., Harrysson, O. and Lewandowski, J. J. (2016). Overview of materials qualification needs for metal additive manufacturing. Jom, 68(3), pp. 747-764. DOI: 10.1007/s11837-015-1810-0.

[4] DebRoy, T., Wei, H. L., Zuback, J. S., Mukherjee, T., Elmer, J. W., Milewski, J. O. and Zhang, W. (2018). Additive manufacturing of metallic components–process, structure and properties. Prog. Mater. Sci., 92, pp. 112-224. DOI: 10.1016/j.pmatsci.2017.10.001.

[5] Lewandowski J.J. and Seifi, M. (2016). Metal additive manufacturing: A review of mechanical properties, Annu. Rev. Mater. Res., 46 (1), pp. 151–186. DOI: /10.1146/annurev-matsci-070115-032024.

[6] Herzog, D., Seyda, V., Wycisk, E. and Emmelmann, C. (2016). Additive manufacturing of metals. Acta Mater. 117, pp. 371-392. DOI: /10.1016/j.actamat.2016.07.019.

[7] Suryawanshi, J., Prashanth, K. G. and Ramamurty, U. (2017). Mechanical behavior of selective laser melted 316L stainless steel. Mater. Sci. Eng. A., 696, pp. 113-121. DOI: 10.1016/j.msea.2017.04.058.

[8] Sun, Z., Tan, X., Tor, S. B. and Chua, C. K. (2018). Simultaneously enhanced strength and ductility for 3D-printed stainless steel 316L by selective laser melting. NPG Asia Mater., 10(4), pp.127-136. DOI: 10.1038/s41427-018-0018-5.

[9] Tan, C., Zhou, K., Ma, W., Zhang, P., Liu, M. and Kuang, T. (2017). Microstructural evolution, nanoprecipitation behavior and mechanical properties of selective laser melted high-performance grade 300 maraging steel. Mater. Des., 134, pp.23-34. DOI: 10.1016/j.matdes.2017.08.026.

[10] Qiu C., Al Kindi M., Aladawi A.S. and Al Hatmi I.. (2018). A comprehensive study on microstructure and tensile behavior of a selectively laser melted stainless steel, Sci. Rep., 8 (1), pp.1-16. DOI: 10.1038/s41598-018-26136-7.

[11] Wang X., Muz-Lerma J.A., Attarian Shandiz M., Sanchez-Mata O. and Brochu M. (2019). Crystallographic-orientation-dependent tensile behaviours of stainless steel 316L fabricated by laser powder bed fusion, Mater. Sci. Eng. A., 766, 138395. DOI: 10.1016/j.msea.2019.138395.

[12] Yin Y.J., Sun J.Q., Guo J., Kan X.F. and Yang D.C. (2019). Mechanism of high yield strength and yield ratio of 316 L stainless steel by additive manufacturing, Mater. Sci. Eng. A., 744, pp.773–777. DOI: 10.1016/j.msea.2018.12.092.

[13] Chen W., Voisin T., Zhang Y., Florien J.-B., Spadaccini C.M., McDowell D.L., Zhu T. and Wang Y.M. (2019). Microscale residual stresses in additively manufactured stainless steel, Nat. Commun., 10(1), pp.1–12. DOI: 10.1038/s41467-019-12265-8.

[14] Maskery, I., Aboulkhair, N. T., Corfield, M. R., Tuck, C., Clare, A. T., Leach, R. K. and Hague, R. J. (2016). Quantification and characterisation of porosity in selectively laser melted Al–Si10–Mg using X-ray computed tomography. Mater. Charact., 111, pp. 193-204. DOI: 10.1016/j.matchar.2015.12.001.

[15] Kim, F. H., Moylan, S. P., Garboczi, E. J. and Slotwinski, J. A. (2017). Investigation of pore structure in cobalt chrome additively manufactured parts using X-ray computed tomography and three-dimensional image analysis. Addit. Manuf., 17, pp. 23-38. DOI: 10.1016/j.addma.2017.06.011.

[16] Blaber, J., Adair, B. and Antoniou, A. (2015). Ncorr: open-source 2D digital image correlation matlab software. Exp. Mech., 55(6), pp. 1105-1122. DOI: 10.1007/s11340-015-0009-1.

[17] Kempen K., Yasa E., Thijs L., Kruth J.-P and van Humbeeck J. (2011). Microstructure and mechanical properties of selective laser melted 18Ni-300 steel, Phys. Procedia., 12, pp. 255–263. DOI: 10.1016/j.phpro.2011.03.033.

[18] Liu, W., Chen, C., Shuai, S., Zhao, R., Liu, L., Wang, X. and Ren, Z. (2020). Study of pore defect and mechanical properties in selective laser melted Ti6Al4V alloy based on X-ray computed tomography. Mater. Sci. Eng. A., 797, 139981. DOI: 10.1016/j.msea.2020.139981.

[19] Cherry J., Davies H., Mehmood S., Lavery N., Brown S. and Sienz J. (2015). Investigation into the effect of process parameters on microstructural and physical properties of 316L stainless steel parts by selective laser melting, Int. J. Adv. Manuf. Technol., 76, pp. 869–879. DOI: 10.1007/s00170-014-6297-2.

[20] Zinoviev, A., Zinovieva, O., Ploshikhin, V., Romanova, V. and Balokhonov, R. (2016). Evolution of grain structure during laser additive manufacturing. Simulation by a cellular automata method. Mater. Des., 106, pp. 321-329. DOI: /10.1016/j.matdes.2016.05.125.

[21] Han, Z., Tang, L. C., Xu, J. and Li, Y. (2009). A three-parameter Weibull statistical analysis of the strength variation of bulk metallic glasses. Scr. Mater., 61(9), pp. 923-926. DOI: 10.1016/j.scriptamat.2009.07.038.

[22] Williams, P. T., Bowman, K. O., Bass, B. R. and Dickson, T. L. (2001). Weibull statistical models of K_{Ic}/K_{Ia} fracture toughness databases for pressure vessel steels with an application to pressurized thermal shock assessments of nuclear reactor pressure vessels. Int. J. Press. Vessel. Pip., 78(2-3), pp. 165-178. DOI: 10.1016/S0308-0161(01)00031-X.

[23] Zahedi, H., Emamy, M., Razaghian, A., Mahta, M., Campbell, J. and Tiryakioğlu, M. (2007). The effect of Fe-rich intermetallics on the Weibull distribution of tensile properties in a cast Al-5% Si-3% Cu-1% Fe-0.3% Mg alloy. Metall. Mater. Trans. A, 38(3), pp. 659-670. DOI: 10.1007/s11661-006-9068-3.

[24] Boyce, B. L. (2010). A sequential tensile method for rapid characterization of extreme-value behavior in microfabricated materials. Exp. Mech., 50(7), pp. 993-997. DOI: 10.1007/s11340-009-9286-x.

[25] Hosford, W. F. and Caddell, R. M. (2011). Metal forming: mechanics and metallurgy. Cambridge university press. DOI: 10.1017/CBO9780511811111.

[26] Ladani, L., Razmi, J. and Farhan Choudhury, S. (2014). Mechanical anisotropy and strain rate dependency behavior of Ti6Al4V produced using E-beam additive fabrication. J. Eng. Mater. Technol., 136(3). DOI: 10.1115/1.4027729.